The Astronomical Journal, 131:2373–2382, 2006 May

THE EXTENDED CHANDRA DEEP FIELD–SOUTH SURVEY: X-RAY POINT-SOURCE CATALOG

Shanil N. Virani, Ezequiel Treister,[1,2] C. Megan Urry,[1] and Eric Gawiser[1,3]
Department of Astronomy, Yale University, P.O. Box 208101, New Haven, CT 06520; svirani@astro.yale.edu
Received 2005 June 23; accepted 2006 January 29

ABSTRACT

The Extended Chandra Deep Field–South (ECDFS) survey consists of four *Chandra X-Ray Observatory* ACIS-I pointings and covers ≈1100 arcmin^2 (≈0.3 deg^2) centered on the original CDF-S field to a depth of approximately 228 ks. This is the largest *Chandra* survey ever conducted at such depth, and only one *XMM-Newton* survey reaches a lower flux limit in the hard 2.0–8.0 keV band. We detect 651 unique sources: 587 using a conservative source-detection threshold and 64 using a lower source-detection threshold. These are presented as two separate catalogs. Of the 651 total sources, 561 are detected in the full 0.5–8.0 keV band, 529 in the soft 0.5–2.0 keV band, and 335 in the hard 2.0–8.0 keV band. For point sources near the aim point, the limiting fluxes are approximately 1.7×10^{-16} and 3.9×10^{-16} ergs cm^{-2} s^{-1} in the 0.5–2.0 and 2.0–8.0 keV bands, respectively. Using simulations, we determine the catalog completeness as a function of flux and assess uncertainties in the derived fluxes due to incomplete spectral information. We present the differential and cumulative flux distributions, which are in good agreement with the number counts from previous deep X-ray surveys and with the predictions from an active galactic nucleus (AGN) population synthesis model that can explain the X-ray background. In general, fainter sources have harder X-ray spectra, consistent with the hypothesis that these sources are mainly obscured AGNs.

Key words: cosmology: observations — diffuse radiation — galaxies: active — surveys — X-rays: galaxies — X-rays: general

Online material: machine-readable tables

1. INTRODUCTION

Wide-area X-ray surveys have played a fundamental role in understanding the nature of the sources that populate the X-ray universe. Early surveys like the *Einstein* Medium Sensitivity Survey (Gioia et al. 1990), the *ROSAT* International X-Ray/Optical Survey (Ciliegi et al. 1997), and the *ASCA* Large Sky Survey (Akiyama et al. 2000) showed that the vast majority of bright X-ray sources are active galactic nuclei (AGNs). More specifically, shallow wide-area surveys in the soft (0.5–2.0 keV) X-ray band yield mostly unobscured, broad-line AGNs, which are characterized by a soft X-ray spectrum with a photon index of $\Gamma \simeq 1.9$ (Nandra & Pounds 1994). In contrast, deep X-ray surveys, particularly surveys that make use of the unprecedented subarcsecond spatial resolution of the *Chandra X-Ray Observatory*, find AGNs with harder X-ray spectra ($\Gamma \sim 1.4$) at fainter fluxes, more like the hard spectrum of the X-ray background.

Deep *Chandra* surveys have thus opened a new vista on resolving the X-ray background and identifying the role and evolution of accretion power in all galaxies. The cosmic X-ray background is now almost completely resolved (∼70%–90%) into discrete sources in the deep pencil-beam surveys like the Chandra Deep Fields (CDF-N, Brandt et al. 2001; CDF-S, Giacconi et al. 2002). To understand the composition of the sources that make up the X-ray background, population synthesis models have been constructed (Madau et al. 1994; Comastri et al. 1995; Gilli et al. 1999, 2001; Treister & Urry 2005) that typically require approximately 3 times as many obscured AGNs as traditional type 1 (unobscured) AGNs.

While the deep fields provide the deepest view of the X-ray universe and have generated plentiful AGN samples at lower luminosities, the small area covered by pencil-beam surveys means luminous sources are poorly sampled. In an attempt to determine the luminosity function of X-ray-emitting AGNs up to $z \sim 5$, as well as to leverage existing deep multiwavelength data in the extended $30' \times 30'$ field centered on the CDF-S, the region surrounding the CDF-S was recently observed by *Chandra*. Covering ≈1100 arcmin^2 (≈0.3 deg^2), the Extended Chandra Deep Field–South (ECDFS) survey is the largest *Chandra* survey field at this depth (≈230 ks) and is the second deepest and widest survey ever conducted in the X-ray (the *XMM-Newton* survey of the Lockman Hole is deeper in the hard band and has ∼30% more area; Hasinger 2004).

In this paper we present the X-ray catalog for the ECDFS and the number counts in two energy bands. In subsequent papers we will present the optical and near-IR properties of these X-ray sources, including first results from our deep optical spectroscopy campaign obtained as part of the 1 deg^2 Multiwavelength Survey by Yale/Chile (MUSYC; Gawiser et al. 2006).

In § 2 we describe our data reduction procedure. In § 3 we describe the point-source detection and astrometry. The X-ray source catalog and basic survey results are presented in § 4, and the conclusions are given in § 5. The average Galactic column density along this line of sight for the four pointings is 9.0×10^{19} cm^{-2} (Stark et al. 1992). We adopt $H_0 = 70$ km s^{-1} Mpc^{-1}, $\Omega_M = 0.3$, and $\Omega_\Lambda = 0.7$ throughout this paper, which is consistent with the cosmological parameters reported by Spergel et al. (2003). All coordinates throughout this paper are J2000.0.

2. OBSERVATIONS AND DATA REDUCTION

2.1. *Instrumentation and Diary of Observations*

All nine observations of the ECDFS survey field were conducted with the Advanced CCD Imaging Spectrometer (ACIS)

[1] Yale Center for Astronomy and Astrophysics, Yale University, P.O. Box 208121, New Haven, CT 06520.
[2] Departamento de Astronomia, Universidad de Chile, Casilla 36-D, Santiago, Chile.
[3] NSF Astronomy and Astrophysics Postdoctoral Fellow.

TABLE 1
JOURNAL OF *Chandra* OBSERVATIONS OF THE ECDFS

Obs. ID	Obs. Start	Exposure Time (ks)		Aim Point		Roll Angle (deg)	CCDs Clocked
		Raw	Filtered	$\alpha_{J2000.0}$	$\delta_{J2000.0}$		
5015	2004 Feb 29	162.9	154.8	03 33 05.61	−27 41 08.84	270.2	I0–I3
5016	2004 Mar 3	77.2	76.8	03 33 05.61	−27 41 08.88	270.2	I0–I3
5017	2004 May 14	155.4	135.2	03 31 51.43	−27 41 38.80	181.5	I0–I3
5018	2004 May 16	72.0	70.2	03 31 51.43	−27 41 38.79	181.5	I0–I3
5019	2004 Nov 17	163.1	162.3	03 31 49.94	−27 57 14.56	0.2	I0–I3, S2
5020	2004 Nov 15	77.6	76.9	03 31 49.94	−27 57 14.56	0.2	I0–I3, S2
5021	2004 Nov 13	97.8	94.2	03 33 02.93	−27 57 16.08	0.2	I0–I3, S2
5022	2004 Nov 15	79.1	75.8	03 33 02.94	−27 57 16.07	0.2	I0–I3, S2
6164	2004 Nov 20	69.1	67.3	03 33 02.93	−27 57 16.04	0.2	I0–I3, S2

NOTE.—Units of right ascension are hours, minutes, and seconds, and units of declination are degrees, arcminutes, and arcseconds.

on board *Chandra* (*Chandra* X-Ray Center 2005)[4] as part of the approved guest observer program in Cycle 5 (proposal number 05900218, principal investigator (PI) N. Brandt; Lehmer et al. 2005). ACIS consists of 10 CCDs, distributed in a 2×2 array (ACIS-I) and a 1×6 array (ACIS-S). All four of the ACIS-I CCDs are front-illuminated CCDs; two of the six ACIS-S CCDs are back-illuminated CCDs (S1 and S3). Of these 10 CCDs, at most six can be operated at any one time. Table 1 presents a journal of the *Chandra* observations of the ECDFS. All nine observations were conducted in Very Faint mode (see *Chandra* X-Ray Center 2005, p. 100) so that the pixel values of the 5×5 event island are telemetered rather than just the 3×3 event island as in Faint mode. This telemetry format offers the advantage of further reducing the instrument background after ground processing (see § 2.2). Observation IDs (ObsIDs) 5019–5022 and 6164 also had the ACIS-S2 CCD powered on (see Table 1). However, due to the large off-axis angle of the S2 CCD during these observations, it has a much broader point-spread function (PSF) and hence lower sensitivity, so we exclude data from this CCD and focus only on data collected from the ACIS-I CCDs. The on-axis CCD for each ACIS-I observation is I3, and the ACIS-I field of view is $16.'9 \times 16.'9$.

2.2. *Data Reduction*

All data were reprocessed using the latest version of the *Chandra* Interactive Analysis of Observations[5] (CIAO, ver. 3.2.1, released 2005 February 10) software, as well as version 3.0.0 of the calibration database (CALDB, released 2004 December 12). We chose to rereduce all nine data sets rather than simply use the standard data processing (SDP) level 2 event files because we wanted the data sets to be reduced in a consistent manner, and, more importantly, we wanted to take advantage of better *Chandra* X-Ray Center (CXC) algorithms to reduce the ACIS particle background by using the information located in the outer 16 pixels of the 5×5 event island,[6] as well as executing a new script that is much more efficient at identifying ACIS "hot pixels" and cosmic-ray afterglow events.[7] This new hot pixel and cosmic-ray afterglow tool is now implemented in the SDP pipeline at the CXC but was not applied in the SDP pipeline of the present observations.

The following procedure was used to arrive at a new level 2 event file. Before applying the new CIAO tool to identify ACIS hot pixels and cosmic-ray afterglow events, the pixels identified in the CXC-provided level 1 event file as being due to a cosmic-ray afterglow event were reset. An afterglow is the residual charge from the interaction of a cosmic ray in a front-side-illuminated CCD frame. Some of the excess charge is captured by charge traps created by the radiation damage suffered early in the mission (see Townsley et al. 2000 and references therein) and released over the next few to few dozen frames. If these afterglow events are not removed from the data, they can result in the spurious detection of faint sources. To better account for such events, a new, more precise method for identifying afterglow events was developed by the CXC and has now been introduced into the SDP pipeline. This CIAO tool, *acis_run_hotpix*, was then run on the reset level 1 event file to identify and flag hot pixels and afterglow events in all nine ACIS observations of the ECDFS. The last step in producing the new level 2 event file was to run the CIAO tool *acis_process_events*. In addition to applying the newest gain map supplied in the latest release of the CALDB, this tool also applies the pixel randomization and the ACIS charge transfer inefficiency (CTI) correction. The latter corrects the data for radiation damage sustained by the CCDs early in the mission. All of these corrections are part of the standard data processing and are on by default in *acis_process_events*. The time-dependent gain correction is also applied to the event list to correct the pulse-invariant energy channel for the secular drift in the average pulse-height amplitude values. This drift is caused primarily by gradual degradation of the CTI of the ACIS CCDs (e.g., Schwartz & Virani, 2004). Finally, the observation-specific bad pixel map created by *acis_run_hotpix* was supplied, and the option to clean the ACIS particle background by making use of the additional pixels telemetered in Very Faint mode was turned on.

Once a new level 2 event file was produced, we applied the standard grade filtering to each observation, choosing only event grades 0, 2, 3, 4, and 6 (the standard *ASCA* grade set), and the standard good time intervals supplied by the SDP pipeline. We also restricted the energy range to 0.5–8.0 keV, as the background rises steeply below and above those limits.[8] Finally, we examined the background light curves for all nine observations, as the ACIS background is known to vary significantly. For example, Plucinsky & Virani (2000) found that the front-illuminated CCDs can show typical increases of 1–5 counts s^{-1} above the quiescent level, while

[4] The *Chandra* Proposers' Guide is also available in HTML format at http://cxc.harvard.edu/proposer/POG/html.
[5] See http://cxc.harvard.edu/ciao.
[6] See "Reducing ACIS Quiescent Background Using Very Faint Mode," http://cxc.harvard.edu/cal/Acis/Cal_prods/vfbkgrnd/index.html.
[7] See http://cxc.harvard.edu/ciao/threads/acishotpixels.
[8] See http://cxc.harvard.edu/contrib/maxim/stowed.

TABLE 2
Exposure Time per Pointing

Pointing	ObsIDs	Raw Exposure (ks)	Net Exposure (ks)
Northeast	5015, 5016	240.1	231.6
Northwest	5017, 5018	227.4	205.4
Southeast	5021, 5022, 6164	240.7	237.4
Southwest	5019, 5020	246.0	239.2
Mean	...	238.6	228.4

the back-illuminated CCDs can show large excursions—as high as 100 counts s^{-1} above the quiescent level—during background flares. The durations of these intervals of enhanced background are highly variable, ranging from 500 to 10^4 s. The cause of these background flares is currently not known (see Grant et al. 2002); however, they may be caused by low-energy protons ($<$100 keV; e.g., Plucinsky & Virani 2000; Strüder et al. 2001). The time periods corresponding to these background flares are generally excised from the data before proceeding with further analysis, although not always (see Brandt et al. 2001; Nandra et al. 2005). In fact, Kim et al. (2004) find that the source detection probability depends strongly on the background rate. To examine our observations for such periods, we used the CIAO script ANALYSE_LTCRV.SL, which identifies periods during which the background is $\pm 3\ \sigma$ from the mean. All nine observations were filtered according to this prescription (see Table 1 for a comparison of raw exposure time vs. filtered exposure time), resulting in only $\sim$40.6 ks ($\sim$4%) being lost due to background flares (954.2 vs. 913.6 ks). Of this, 20.3 ks were excluded from the end of ObsID 5017 due to a flare in which the count rate increased by a factor of $\sim$2. Table 2 lists the net exposure time for each of the four pointings used to image the ECDFS region. The net exposure time for each of the four pointings varies from a low of 205 ks to a high of 239 ks, with the mean net exposure time for the entire survey field of 228 ks. These extra steps in processing help remove spurious sources and result in fewer catalog sources than if the standard processing or pipeline products were used.

3. DATA ANALYSIS

In this paper we report on the sources detected in three standard X-ray bands (see Table 3): 0.5–8.0 keV (full band), 0.5–2.0 keV (soft band), and 2.0–8.0 keV (hard band). The raw ACIS resolution is $0\farcs492$ $pixel^{-1}$; however, source detection and flux determinations were performed on the block 4 images, i.e., $1\farcs964$ $pixel^{-1}$, as the source-detect tool and exposure map generation require significant computer resources for full-size images. For greater accuracy, source positions were determined from the block 1 images.

3.1. *Image and Exposure Map Creation*

Observations at each of the four pointings were combined via the CIAO script *merge_all*. This script was executed using CIAO, version 2.3, because of a known bug in the *asphist* tool under CIAO, version 3.2.1; this bug results in incorrect exposure maps for the merged image.[9] At each pointing, the observation with the longest integration time was used for coordinate registration. For example, when merging ObsIDs 5015 and 5016, the merged event list was registered to ObsID 5015, as it has approximately twice the integration time as 5016. Table 2 lists the ObsIDs for each pointing, as well as the raw and the net integration time. For each pointing, we constructed images in the three standard bands: the full band, soft band, and hard band; see Table 3. The full-band exposure-corrected image for the entire survey field[10] is presented in Figure 1.

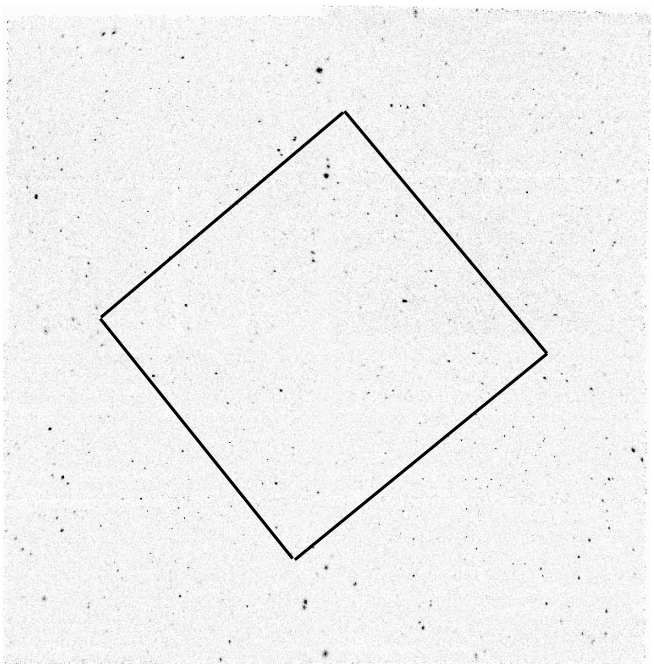

Fig. 1.—Exposure-corrected full-band (0.5–8.0 keV) image of the ECDFS. This image has been binned by a factor of 4 in both right ascension and declination and was made using the standard *ASCA* grade set. The black square superposed on the raw image is the approximate footprint (most of the exposure lies within this region) of the CDF-S proper (Giacconi et al. 2002).

We constructed exposure maps in these three energy bands for each pointing and for the entire survey field.[11] These exposure maps were created in the standard way and are normalized to the effective exposure of a source location at the aim point. The procedure used to create these exposure maps accounts for the effects of vignetting, gaps between the CCDs, bad column filtering, and bad pixel filtering. However, it should be noted that charge blooms caused by cosmic rays can reduce the detector efficiency by as much as a few percent.[12] There is currently no way to account for such charge cascades; however, when a tool becomes available, we will correct for this effect as necessary and make the new exposure maps publicly available at our Web site.[13] The exposure maps were binned by four so that they were congruent to the final reduced images. A photon index of $\Gamma = 1.4$, the slope of the X-ray background in the 0.5–8.0 keV band (e.g., Marshall et al. 1980; Gendreau et al. 1995; Kushino et al. 2002), was used in creating these exposure maps.

TABLE 3
Definition of Energy Bands and Hardness Ratio

Name	Definition
Full band (F)	0.5–8.0 keV
Soft band (S)	0.5–2.0 keV
Hard band (H)	2.0–8.0 keV
Hardness ratio (HR)	$(H - S)/(H + S)$

[9] See the usage warning at http://cxc.harvard.edu/ciao/threads/merge_all.
[10] Raw and smoothed *ASCA*-grade images for all three standard bands (see Table 3) are available from http://www.astro.yale.edu/svirani/ecdfs.
[11] Exposure maps for all three standard bands (see Table 3) are available from http://www.astro.yale.edu/svirani/ecdfs.
[12] See http://cxc.harvard.edu/ciao/caveats/acis_caveats_050620.html.
[13] See footnote 11.

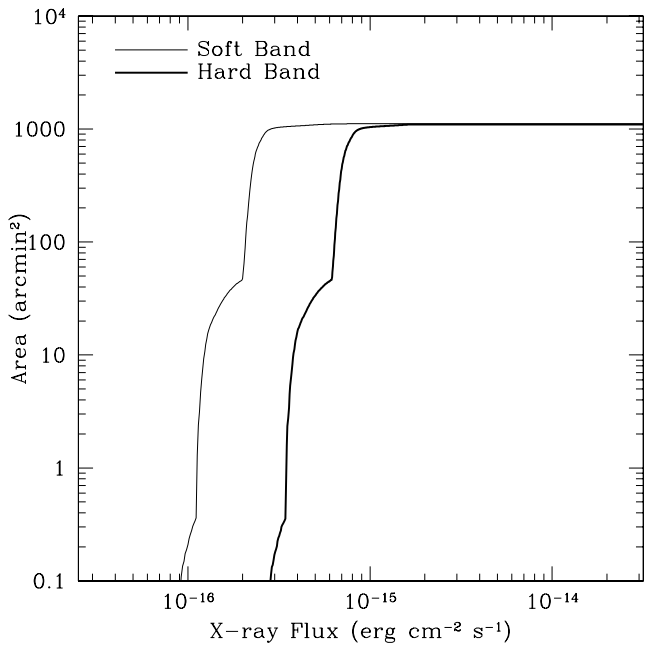

FIG. 2.—Survey area vs. limiting flux for the two bands for which we have calculated the $\log N$-$\log S$ function: soft band (*thin line*) and hard band (*thick line*). The total area of the survey is ≈1100 arcmin^2 (∼0.3 deg^2).

In order to calculate the survey area as a function of the X-ray flux in the soft and hard bands, we used the exposure maps generated for each band and assumed a fixed detection threshold of 5 counts in the soft band and 2.5 in the hard band (∼2 σ). Dividing these counts by the exposure map, we obtain the flux limit at each pixel for each band. The pixel area is then converted into a solid angle, and the cumulative histogram of the flux limit is constructed (Fig. 2). The total survey area is ≈1100 arcmin^2 (≈0.3 deg^2). A more precise method of determining the survey area as a function of the X-ray flux is described by Kenter & Murray (2003); however, this would affect only the faint tail of the sample and would not significantly alter the present results. Therefore, a more sophisticated treatment is deferred to a later paper.

3.2. *Point-Source Detection*

To perform X-ray source detection, we applied the CIAO wavelet detection algorithm *wavdetect* (Freeman et al. 2002). Although several other methods have been used in other survey fields to find sources in *Chandra* observations (e.g., Giacconi et al. 2002; Nandra et al. 2005), we chose *wavdetect* to allow a straightforward comparison between sources found in our catalog and those found in the CDF-S (Giacconi et al. 2002; Alexander et al. 2003). Moreover, *wavdetect* is more robust in detecting individual sources in crowded fields and in identifying extended sources than the other CIAO detection algorithm, *celldetect*. Point-source detection was performed in each standard band (see Table 3) using a "$\sqrt{2}$ sequence" of wavelet scales; scales of 1, $\sqrt{2}$, 2, $2\sqrt{2}$, 4, $4\sqrt{2}$, and 8 pixels were used. Brandt et al. (2001), for example, showed that using larger scales can detect a few additional sources at large off-axis angles but found that this $\sqrt{2}$ sequence gave the best overall performance across the CDF-N field. Moreover, as Alexander et al. (2003) point out, sources found with larger scales tend to have source properties and positions too poorly defined to give useful results.

Our criterion for source detection is that a source must be found with a false-positive probability threshold ($p_{\rm thresh}$) of 1×10^{-7} in at least one of the three standard bands. This false-positive probability threshold is typical for point-source catalogs (e.g., Alexander et al. 2003; Wang et al. 2004), although Kim et al. (2004) found that a significance threshold parameter of 1×10^{-6} gave the most efficient results in the *Chandra* Multiwavelength Project survey. We ran *wavdetect* using both probability thresholds and found that using the lower significance threshold (i.e., 1×10^{-6}) results in only an additional 64 unique sources. Visual inspection of each of these sources suggests they are bona fide X-ray sources. However, because these are sources found with the lower significance threshold, we present them in a separate table (the secondary catalog; Table 5). The primary catalog (Table 4) is a compilation of 587 unique sources found using the higher significance threshold in at least one of the three energy bands. For the remaining source detection parameters, we used the default values specified in CIAO, which included requiring that a minimum of 10% of the on-axis exposure was needed in a pixel before proceeding to analyze it. We also applied the exposure maps generated for each pointing (see § 3.1) to mitigate finding spurious sources, which are most often located at the edge of the field of view.

The number of spurious sources per pointing is approximately $p_{\rm thresh} \times N_{\rm pix}$, where $N_{\rm pix}$ is the total number of pixels in the image, according to the *wavdetect* documentation. Since there are approximately 2×10^6 pixels in each image for each pointing, we expect ∼0.2 spurious sources per pointing per band for a probability threshold of 1×10^{-7}. Therefore, treating the 12 images searched as independent, we expect ∼2–3 false sources in our primary catalog (Table 4) for the case of a uniform background. Of course the background is neither perfectly uniform nor static as the level decreases in the gaps between the CCDs and increases slightly near bright point sources. As mentioned by Brandt et al. (2001) and Alexander et al. (2003), one might expect the number of false sources to be increased by a factor of ∼2–3 due to the large variation in effective exposure time across the field and the increase in background near bright sources due to the point-spread function (PSF) wings. But our false-source estimate is likely to be conservative by a similar factor since *wavdetect* suppresses fluctuations on scales smaller than the PSF. That is, a single pixel is unlikely to be considered a source detection cell, particularly at large off-axis angles (Alexander et al. 2003).

The source lists generated by the procedure above for each of the standard bands in each of the pointings of the ECDFS were merged to create the point-source catalogs presented in Tables 4 and 5. The source positions listed in each catalog are the full-band *wavdetect*-determined positions except when the source was detected only in the soft or hard bands. To identify the same source in the different energy bands, a matching radius of 2.″5 or twice the PSF size of each detect cell, whichever was the largest, was used. For comparison, Alexander et al. (2003) and Nandra et al. (2005) used a matching radius of 2.″5 for sources within 6′ of the aim point, and 4.″0 for sources with larger off-axis angles. With our method, nine and three soft- and hard-band sources, respectively, have more than one counterpart, so we took the closest one. Note that both Tables 4 and 5 exclude sources found by *wavdetect* in which one or both of the axes of the "source ellipse" collapsed to zero. Over the survey field, 70 such sources are found; in general, these are unusual sources, and although the formal probability of being spurious is low, there may be problems with these detections. Hornschemeier et al. (2001) found that using the *wavdetect*-determined counts for such objects as we do results in a gross underestimate of the number of counts even though the source was detected with a probability threshold of 1×10^{-7}. Since these sources would appear in catalogs that do

TABLE 4

PRIMARY CATALOG OF X-RAY SOURCES IN THE ECDFS FIELD ($p_{\rm thresh} = 1 \times 10^{-7}$).

					COUNT RATE												
					FULL BAND			SOFT BAND			HARD BAND						
ID	NAME (CXOYECDF)	R.A. (J2000.0)	DECL. (J2000.0)	PSF (arcsec)	Value	Upper	Lower	Value	Upper	Lower	Value	Upper	Lower	FB FLUX[a] (ergs cm^{-2} s^{-1})	SB FLUX[a] (ergs cm^{-2} s^{-1})	HB FLUX[a] (ergs cm^{-2} s^{-1})	NOTES
(1)	(2)	(3)	(4)	(5)	(6)	(7)	(8)	(9)	(10)	(11)	(12)	(13)	(14)	(15)	(16)	(17)	(18)
1.....	J033335.6−273935	03 33 35.56	−27 39 35.3	1.75	7.64e−04	8.26e−04	7.07e−04	5.05e−04	5.56e−04	4.59e−04	...	...	...	9.16e−15	2.95e−15	6.44e−15	...
2.....	J033334.9−274209	03 33 34.93	−27 42 08.5	1.64	9.00e−03	9.20e−03	8.80e−03	...	...	...	2.88e−03	3.00e−03	2.77e−03	1.08e−13	3.30e−14	6.38e−14	...
3.....	J033332.9−274011	03 33 32.92	−27 40 11.2	1.45	2.16e−04	2.51e−04	1.85e−04	1.94e−04	2.28e−04	1.65e−04	...	...	...	2.59e−15	1.14e−15	1.82e−15	...
4.....	J033332.8−274908	03 33 32.79	−27 49 08.0	4.05	1.81e−03	1.91e−03	1.73e−03	1.06e−03	1.13e−03	9.95e−04	4.45e−04	4.93e−04	4.01e−04	2.17e−14	6.21e−15	9.83e−15	...
5.....	J033329.8−274009	03 33 29.84	−27 40 09.1	1.17	3.45e−04	3.89e−04	3.07e−04	1.81e−04	2.14e−04	1.54e−04	...	...	...	4.14e−15	1.06e−15	2.91e−15	...

NOTES.—Units of right ascension are hours, minutes, and seconds, and units of declination are degrees, arcminutes, and arcseconds. Table 4 is published in its entirety in the electronic edition of the *Astronomical Journal*. A portion is shown here for guidance regarding its form and content.

[a] Flux corrected for Galactic absorption with $N_{\rm H} = 9 \times 10^{19}$ cm^{-2}, assuming $\Gamma = 1.4$.

TABLE 5

SECONDARY CATALOG OF X-RAY SOURCES IN THE ECDFS FIELD ($p_{\rm thresh} = 1 \times 10^{-6}$).

					COUNT RATE												
					FULL BAND			SOFT BAND			HARD BAND						
ID	NAME (CXOYECDF)	R.A. (J2000.0)	DECL. (J2000.0)	PSF (arcsec)	Value	Upper	Lower	Value	Upper	Lower	Value	Upper	Lower	FB FLUX[a] (ergs cm^{-2} s^{-1})	SB FLUX[a] (ergs cm^{-2} s^{-1})	HB FLUX[a] (ergs cm^{-2} s^{-1})	NOTES
(1)	(2)	(3)	(4)	(5)	(6)	(7)	(8)	(9)	(10)	(11)	(12)	(13)	(14)	(15)	(16)	(17)	(18)
1.....	J033331.7−273850	03 33 31.70	−27 38 50.3	0.75	1.34e−04	1.63e−04	1.10e−04	...	...	...	...	...	...	1.61e−15	4.91e−16	1.13e−15	f
2.....	J033329.0−274558	03 33 28.97	−27 45 58.1	0.93	2.38e−04	2.74e−04	2.06e−04	...	...	...	...	...	...	2.85e−15	8.70e−16	2.00e−15	f
3.....	J033326.4−273522	03 33 26.36	−27 35 22.4	1.06	1.43e−04	1.72e−04	1.18e−04	...	...	...	...	...	...	1.71e−15	5.22e−16	1.20e−15	...
4.....	J033323.9−273828	03 33 23.91	−27 38 27.8	0.47	1.30e−04	1.58e−04	1.06e−04	...	...	...	...	...	...	1.55e−15	4.75e−16	1.09e−15	f
5.....	J033231.2−273919	03 32 31.18	−27 39 18.5	1.23	3.37e−04	3.79e−04	2.99e−04	6.48e−05	8.62e−05	4.83e−05	...	...	...	4.04e−15	3.78e−16	2.84e−15	...

NOTES.—Units of right ascension are hours, minutes, and seconds, and units of declination are degrees, arcminutes, and arcseconds. Table 5 is published in its entirety in the electronic edition of the *Astronomical Journal*. A portion is shown here for guidance regarding its form and content.

[a] Flux corrected for Galactic absorption with $N_{\rm H} = 9 \times 10^{19}$ cm^{-2} assuming $\Gamma = 1.4$.

TABLE 6
CATALOG OF COLLAPSED *wavdetect* X-RAY SOURCES IN THE ECDFS SURVEY

ID	Name (CXOYECDF)	R.A. (J2000.0)	Decl. (J2000.0)	Notes
1.....	J033208.9−275910	03 32 08.87	−27 59 10.10	Full
2.....	J033203.3−280128	03 32 03.33	−28 01 27.90	Full, hard
3.....	J033201.5−280004	03 32 01.50	−28 00 03.94	Full
4.....	J033151.8−280035	03 31 51.79	−28 00 34.80	Full
5.....	J033150.9−280154	03 31 50.87	−28 01 53.85	Full

NOTES.—Units of right ascension are hours, minutes, and seconds, and units of declination are degrees, arcminutes, and arcseconds. Table 6 is published in its entirety in the electronic edition of the *Astronomical Journal*. A portion is shown here for guidance regarding its form and content.

circular aperture photometry instead, we present this list in a separate catalog (Table 6) for completeness.

Below we define the columns in Tables 4 and 5, our primary and secondary source catalogs for the ECDFS survey.

Column (1) gives the ID number of the source in our catalog.

Column (2) indicates the International Astronomical Union approved names for the sources in this catalog. All sources begin with the acronym "CXOYECDF" (for "Yale E-CDF").[14]

Columns (3) and (4) give the right ascension and declination, respectively. These are *wavdetect*-determined positions for the unbinned images. If a source is detected in multiple bands, then we quote the position determined in the full band; when a source is not detected in the full band, we quote the soft-band position or the hard-band position.

Column (5) gives the PSF cell size, in units of arcseconds, as determined by *wavdetect*. The farther off-axis a source lies, the larger the PSF size.

Columns (6)–(8) give the count rates (in units of counts s^{-1}) in the full band and the corresponding upper and lower error bounds estimated according to the prescription of Gehrels (1986). If a source is undetected in this band, no count rate is tabulated.

Columns (9)–(11) give the count rates (in units of counts s^{-1}) in the soft band and the corresponding upper and lower error bounds estimated according to the prescription of Gehrels (1986). If a source is undetected in this band, no count rate is tabulated.

Columns (12)–(14) give the count rates (in units of counts s^{-1}) in the hard band and the corresponding upper and lower error bounds estimated according to the prescription of Gehrels (1986). If a source is undetected in this band, no count rate is tabulated.

Column (15) lists the full-band flux (in units of ergs cm^{-2} s^{-1}) calculated using a photon slope of $\Gamma = 1.4$ and corrected for Galactic absorption. If a source was undetected in the full band but was detected in the hard or soft band, the hard- or soft-band flux (in that order of priority) was used to extrapolate to the full band assuming a photon slope of 1.4.

Column (16) lists the soft-band flux (in units of ergs cm^{-2} s^{-1}) calculated using a photon slope of $\Gamma = 1.4$ and corrected for Galactic absorption. If a source was undetected in the soft band but was detected in the full or hard band, the full- or hard-band flux (in that order of priority) was used to extrapolate to the soft band assuming a photon slope of 1.4.

Column (17) lists the hard-band flux (in units of ergs cm^{-2} s^{-1}) calculated using a photon slope of $\Gamma = 1.4$ and corrected for Galactic absorption. If a source was undetected in the hard band but was detected in the full or soft band, the full- or soft-band flux (in that order of priority) was used to extrapolate to the hard band assuming a photon slope of 1.4.

Column (18) provides individual notes for each source. Examples include the catalog ID number if detected in the CDF-S by Alexander et al. (2003), or if the source was selected from a band other than the full band ("h" or "s") or was only detected in the full band ("f").

To determine source counts for each of our sources, we extracted counts in the standard bands from each of the images using the geometry of the *wavdetect* source cell and the *wavdetect*-determined source position. For example, to determine the counts in the soft band, we used the position and geometry determined by *wavdetect* in the soft-band image to extract soft-band counts. Some studies use circular aperture photometry to extract source counts. However, as both Hornschemeier et al. (2001) and Yang et al. (2004; see their Fig. 5) demonstrate, both techniques generally return the same result. Net count rates were then calculated using the effective exposure (which includes vignetting) for each pointing (exposure maps generated as described in § 3.1). Errors were derived following Gehrels (1986), assuming an 84% confidence level. Note that the exposure maps do account for the degradation of the soft X-ray response of ACIS due to the buildup of a contamination layer on the ACIS optical blocking filter (Marshall et al. 2004; see § 3.4). Therefore, the count rates reported in Table 4 are exposure- and contamination-corrected.

In Table 7 we summarize the source detections in the three standard bands, and in Table 8 we summarize the number of sources detected in one band but not in another. To convert the count rates to flux, we determined the conversion factor for each band assuming a photon slope of $\Gamma = 1.4$ and the mean Galactic $N_{\rm H}$ absorption along the line of sight for each of the four pointings ($N_{\rm H} = 9 \times 10^{19}$ cm^{-2}; Stark et al. 1992).

Our faintest soft-band sources have ≈4 counts (about one every 1.5 days), and our faintest hard-band sources have ≈6 counts; these sources are detected near the aim point. The corresponding 0.5–2.0 and 2–8 keV flux limits, corrected for the Galactic column density, are $\approx 1.7 \times 10^{-16}$ and $\approx 3.9 \times 10^{-16}$ ergs cm^{-2} s^{-1}, respectively. Of course, these flux limits vary and generally increase across the field of view.

Undoubtedly, there are some sources in Table 4 that are extended sources (i.e., resolved by *Chandra*). Giacconi et al. (2002) find 18 extended sources in their 1 Ms catalog of the CDF-S out of 346 unique sources. The ECDFS survey has approximately 25% the integration time of the CDF-S but is approximately 3 times larger in area. Therefore, we expect roughly the same fraction of our sources reported in Table 4 to be extended. The identification, X-ray, and optical properties of these sources will be presented in a later paper.

3.3. *Astrometry*

Given the superb *Chandra* spatial resolution, the on-axis positional accuracy is often quoted as being accurate to within 1″ (e.g., Kim et al. 2004); in fact, the overall 90% uncertainty circle of a *Chandra* X-ray absolute position has a radius of 0.″6, and the 99% limit on positional accuracy is 0.″8.[15] Nevertheless, as the off-axis angle increases, the PSF broadens and becomes circularly asymmetric (see *Chandra* X-Ray Center 2005). Therefore, source positions for faint sources at large off-axis angles may not

[14] Name registration submitted to http://cdsweb.u-strasbg.fr/viz-bin/DicForm.

[15] See http://cxc.harvard.edu/cal/ASPECT/celmon.

TABLE 7
SUMMARY OF *Chandra* SOURCE DETECTIONS

ENERGY BAND	NUMBER OF SOURCES[a]	DETECTED COUNTS PER SOURCE			
		Maximum	Minimum	Median	Mean
Full band	561	2403.0	2.9	55.4	127.6
Soft band	529	1643.5	4.4	32.4	89.9
Hard band	335	757.4	3.3	42.7	75.2

[a] There are 651 independent X-ray sources detected with a false-positive probability threshold of either 1×10^{-7} (Table 4) or 1×10^{-6} (Table 5).

be accurate. In order to test the astrometry of the *wavdetect*-determined positions, we have matched our full-band X-ray positions provided in Table 4 against deep *BVR*-band imaging produced by MUSYC[16] (Gawiser et al. 2006). The 5 σ depth of the MUSYC optical imaging of this field is 27.1 AB mag with approximately 0.″85 seeing. Correlating the X-ray positions reported in Tables 4 and 5 with the optical positions found for sources in the ECDFS field, we find that approximately 72% of the sources reported in Table 4 and 41% of the sources reported in Table 5 have an optical counterpart within 1.″5 of the X-ray position. Furthermore, comparing the X-ray positions with the optical positions for these matched sources, we find a mean offset of $-0.''08$ in right ascension and $+0.''28$ in declination. (We do not correct the X-ray positions for these offsets.) The optical properties of these X-ray sources will be presented in a forthcoming paper (S. Virani et al. 2006, in preparation).

3.4. *Accuracy of Source Detections and Fluxes*

Approximately one-third of the ECDFS field overlaps with the 1 Ms CDF-S (see Fig. 1 for the field layout). This is very useful, as it allows us to compare our results with the properties of the overlapping sources already published. In particular, we used the catalog of Alexander et al. (2003), who reanalyzed the original CDF-S data. In Figure 3 we show the ratio of our fluxes to those reported by Alexander et al. (2003) for the overlapping sources. For this comparison, neither the CDF-S nor the ECDFS sources were corrected for intrinsic Galactic absorption. (This correction is $\simeq$4% in the soft band and is negligible in the hard band.) Error bars are calculated by adding in quadrature the statistical (Poisson) uncertainties in the counts plus a 10% error arising from the likely range in spectral slopes (see § 3.5).

Sources were matched using the closest CDF-S counterpart to each ECDFS source, using a maximum search radius of $\sim 2''$. To compare the fluxes of matched sources in the two data sets, we excluded the most discrepant top and bottom 15% of the flux ratios, and found that our fluxes are $\sim$14% higher in the soft band and $\sim$11% higher in the hard band. In the first case, the difference can be explained by the different treatment of the contamination layer, which is particularly important in the soft band. The Alexander et al. (2003) catalog used ACISABS[17] to correct their fluxes for the presence of a contamination layer in the ACIS instrument. This tool assumes a spatially uniform contamination layer composed of hydrogen, carbon, nitrogen, and oxygen. However, recent analysis of grating data (Marshall et al. 2004) shows that the amount of contamination correction depends on the spatial position on the instrument, and that the actual composition of the contamination is hydrogen, carbon, oxygen, and fluorine (P. Plucinsky 2005, private communication). These two new discoveries may have caused Alexander et al. (2003) to underestimate the contamination correction, thus making their fluxes lower in the soft band. In the hard band, the discrepancy can be explained by our assumed value of $\Gamma = 1.4$ for the spectral slope to calculate fluxes, while Alexander et al. (2003) used individual spectral fits for most of these overlapping sources. We conclude that the fluxes are broadly consistent and that systematic uncertainties in their average values are $\sim$15%, although individual fluxes have larger uncertainties (and some AGNs may have actually varied).

3.5. *Simulations*

We performed extensive XSPEC and MARX simulations to investigate the statistical properties of the catalog, its completeness, and its flux limits. First, in order to investigate the effect of a fixed photon slope on the true flux of sources found in the ECDFS, we simulated 2000 sources with extreme photon spectral slopes, $\Gamma = 1$ and $\Gamma = 2$, and with fluxes distributed smoothly from the minimum to the maximum in our sample. We then computed their count rates in a typical ECDFS pointing ($\sim$230 ks). Using a fixed photon slope of $\Gamma = 1.4$ to compute fluxes then results in systematic flux errors of $\sim$10% in both the hard and soft bands.

To investigate the completeness of our catalog, we used MARX to simulate X-ray images of sources with known properties, including the range of count rates from just below our threshold to just above our highest count rate, and a generous range of spectral slopes ($1 \leq \Gamma \leq 2$) drawn from the observed Γ distribution observed in the 1 Ms CDFS survey (Alexander et al. 2003). We positioned 1000 sources of known fluxes (consistent with an exposure time of $\sim$230 ks) randomly within the ECDFS survey field, so the background and noise properties of the data are real. We then analyzed these simulated data with the same procedures used on the real ECDFS data; that is, we performed source detection on the resulting event list via *wavdetect*. This resulted in $\sim$90% of the sources being recovered overall, with incompleteness

[16] For more information, see http://www.astro.yale.edu/musyc.

TABLE 8
SOURCES DETECTED IN ONE BAND BUT NOT ANOTHER
(PRIMARY AND SECONDARY TABLES COMBINED)

DETECTION ENERGY BAND	NONDETECTION ENERGY BAND			
	Full	Soft	Hard	Neither
Full	0	113	235	56
Soft	81	0	260	81
Hard	9	65	0	9

NOTE.—For example, there were 113 sources out of 651 that were detected in the full band but not in the soft band.

[17] Available at http://www.astro.psu.edu/users/chartas/xcontdir/xcont.html.

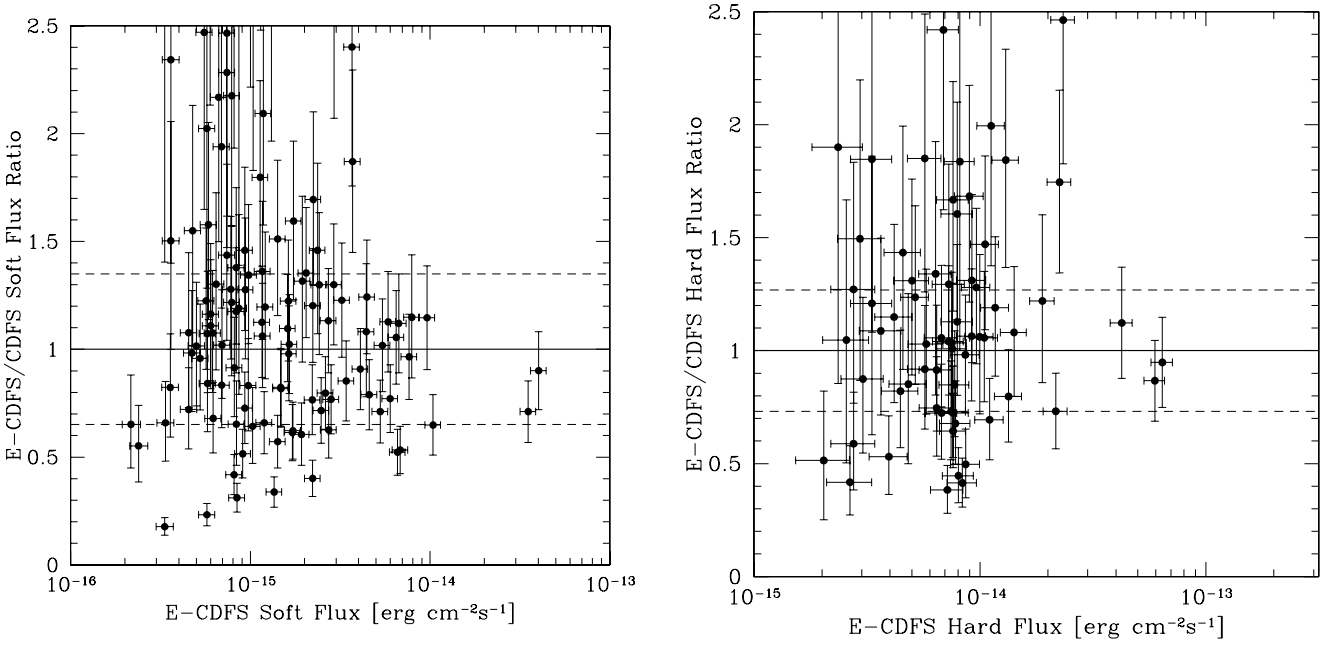

FIG. 3.—Comparison of X-ray fluxes for the 115 soft sources (*left*) and the 89 hard sources (*right*) detected in the CDF-S catalog of Alexander et al. (2003). For this comparison, X-ray fluxes are not corrected for intrinsic Galactic absorption. In general, there is very good agreement between the two independent data sets, with an average flux ratio in the soft band of 1.14, with an rms of 35%, shown by the dashed horizontal lines. In the hard band the average flux ratio is 1.11 with an rms of 27%. These differences are explained by different treatments of the contamination layer and spectral slope and suggest that systematic uncertainties in the flux are ≈10%–15%. Note that some AGNs may have actually varied between these two epochs. Error bars are calculated by adding in quadrature the statistical (Poisson) uncertainties in the counts plus a 10% error arising from the likely range in spectral slopes (see § 3.5).

becoming important below $\sim 2 \times 10^{-16}$ and $\sim 2 \times 10^{-15}$ ergs cm^{-2} s^{-1} in the soft and hard bands, respectively.

4. RESULTS AND DISCUSSION

We found 651 unique sources in the ECDFS survey field, which spans ≈0.3 deg^2 on the sky. Of these, 561 were detected in the 0.5–8.0 keV full band, 529 in the 0.5–2.0 keV soft band, and 335 in the 2.0–8.0 keV hard band. There are 9 hard-band sources that are not detected in either the soft or full bands, 81 soft-band sources not detected in either the hard or full bands, and 56 full-band sources not detected in either the soft or hard bands (see Table 8). Of the 335 hard-band sources, 83 were not detected in

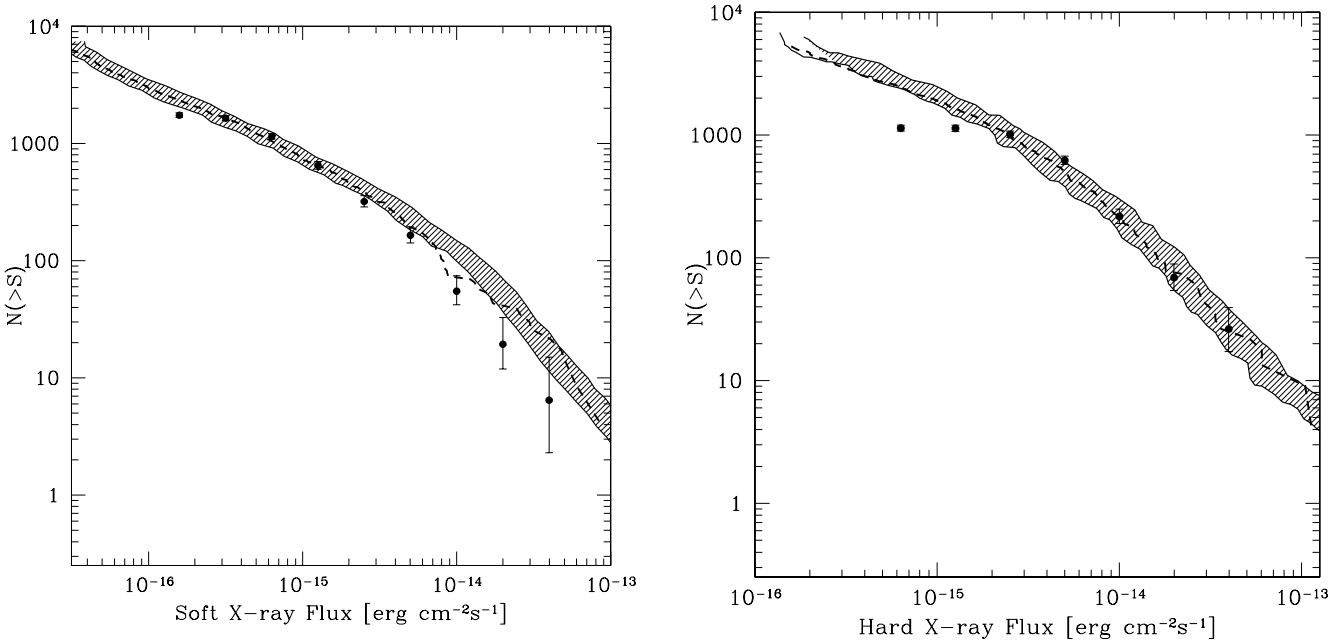

FIG. 4.—Cumulative flux distributions for the soft (*left*) and hard (*right*) bands. Circles present data for the ECDFS catalog, with error bars corresponding to the 84% confidence level (Gehrels 1986). Note that the error bars are not independent. For comparison, we show the log N-log S compiled by Moretti et al. (2003) from *ROSAT*, *ASCA*, *XMM-Newton*, and *Chandra* observations with $\pm 1\ \sigma$ errors (*hatched region*) and the distribution for sources in the CDF-N and CDF-S (Bauer et al. 2004; *dashed line*). The 2–10 keV fluxes of Moretti et al. (2003) and Bauer et al. (2004) were converted to 2–8 keV fluxes using a factor of 0.8, corresponding to a spectral slope of 1.4. The agreement is very good down to fluxes at which incompleteness in the ECDFS catalog becomes important (see § 3.5), $\sim 2 \times 10^{-16}$ and $\sim 2 \times 10^{-15}$ ergs cm^{-2} s^{-1}, in the soft and hard bands, respectively.

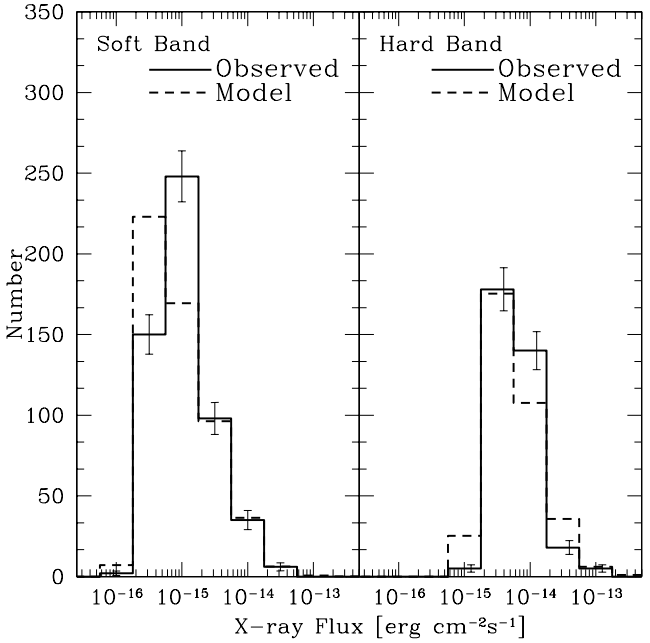

FIG. 5.—Observed differential flux distribution (*solid histogram*) for sources in the ECDFS in the soft (*left*) and hard (*right*) bands, in $\Delta \log S = 0.5$ bins. The distribution (*dashed histogram*) predicted by an AGN unification model that also explains the X-ray background (Treister et al. 2004; Treister & Urry 2005) agrees well in the bright to intermediate flux range for both bands. Below $F_X \sim 3 \times 10^{-16}$ ergs cm^{-2} s^{-1} in the soft band, and $F_X \sim 1 \times 10^{-15}$ ergs cm^{-2} s^{-1} in the hard band, incompleteness in our catalog becomes important.

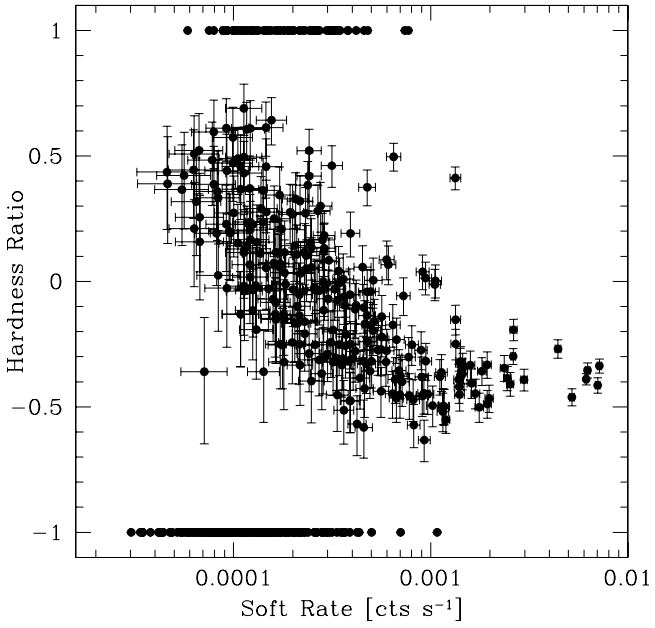

FIG. 6.—Hardness ratio (defined as the ratio of hard minus soft counts to the summed counts) vs. soft X-ray count rate for sources in the ECDFS. Error bars correspond to the 84% confidence level on the count rates (Gehrels 1986). For sources not detected in the soft band (i.e., HR $= +1$) the hard count rate was used instead. Fainter sources in the soft band have harder X-ray spectra, supporting the hypothesis that these sources are mainly obscured AGNs, as required by population synthesis models for the X-ray background.

the soft band ($\sim$20%); these are candidates for highly absorbed sources. Of the 529 and 335 sources detected in the soft and hard bands, respectively, 118 and 73 are detected in the CDF-S itself. Over this 0.11 deg^2 area, with an exposure time of $\sim$1 Ms, Giacconi et al. (2002) found 346 unique sources, of which 307 were detected in the 0.5–2.0 keV band and 251 in the 2–10 keV band. In the CDF-N, with an area similar to the CDF-S but with twice the exposure, Alexander et al. (2003) found 503 X-ray sources in the 2 Ms exposure. The number of sources found in the ECDFS is consistent with these two pencil-beam surveys, given an approximate slope of unity for the X-ray counts in this flux range.

The cumulative distribution of sources for the soft and hard bands is shown in Figure 4. Error bars for a given bin were calculated by adding in quadrature the error bars from the previous bin to the 84% confidence error bars appropriate to the additional number of sources in the present bin, following the procedure described in Gehrels (1986). The observed distribution is compared to the compilation of Moretti et al. (2003) and to the $\log N$-$\log S$ for the *Chandra* deep fields reported by Bauer et al. (2004). In the soft band there is very good agreement with the comparison sample in the flux range from $\sim 4 \times 10^{-14}$ to 2×10^{-16} ergs cm^{-2} s^{-1}. At the bright end, the discrepancy is not statistically significant ($\sim 1\ \sigma$) because there are few bright X-ray sources in our field. At fluxes below $\sim 2 \times 10^{-16}$ ergs cm^{-2} s^{-1}, the observed $\log N$-$\log S$ in the ECDFS flattens relative to the comparison samples because of incompleteness near the flux limit. Sources with soft fluxes of $\leq 2 \times 10^{-16}$ ergs cm^{-2} s^{-1} are only detected at the $\leq 2\ \sigma$ level, and thus not all sources are recovered.

The $\log N$-$\log S$ relation for the hard band is shown in Figure 4 (*right*) and is compared again with the distributions of Moretti et al. (2003) and Bauer et al. (2004). Moretti et al. (2003) used 2–10 keV instead of 2–8 keV for the hard band. To convert 2–10 keV fluxes to the 2–8 keV band, we used a factor of 0.8, corresponding to the flux conversion assuming a $\Gamma = 1.4$ spectral slope. Bauer et al. (2004) quote 2–8 keV but appear to have used 2–10 keV, so we also converted their fluxes by the same factor (which reproduces their curve in Fig. 4 of their paper). As in the soft band, very good agreement with previously reported $\log N$-$\log S$ relations is seen for the 4×10^{-14} to 2×10^{-15} ergs cm^{-2} s^{-1} range, and again, incompleteness at the faint end explains the observed discrepancy.

The differential $\log N$- $\log S$ for both the soft and hard bands is shown in Figure 5. These observed distributions are compared to the predictions of the AGN population synthesis model of Treister & Urry (2005), which explains the X-ray background as a superposition of mostly obscured AGNs. This model also explains the multiwavelength number counts of AGNs in the *Chandra* deep fields (Treister et al. 2004). Given that these models match very well to the observed cumulative flux distributions from existing surveys, it is not surprising that this model also successfully explains the $\log N$-$\log S$ distributions in the ECDFS field. Discrepancies can be found only at the fainter end, where incompleteness causes the number of observed sources to fall below the model prediction.

One of the early *Chandra* results was the finding that fainter X-ray sources have in general harder spectra (Giacconi et al. 2001), represented by higher values of the hardness ratio. Figure 6 shows that this effect is also observed in the ECDFS field, for a much larger number of sources. This trend is explained by obscuration since the soft-band count rate is relatively more affected than the hard band, creating a harder observed X-ray spectrum while at the same time reducing the observed soft flux. This is in accordance with the general picture of AGN unification, although the precise geometry is not constrained, and it is as expected from population synthesis models (e.g., Treister & Urry 2005 and references therein), which require a large number of obscured AGNs

at moderate redshift to explain the spectral shape of the X-ray background.

5. CONCLUSIONS

We present here the X-ray properties of sources detected in deep *Chandra* observations of the ECDFS field, the largest *Chandra* survey ever performed in terms of both area and depth. This survey covers a total of 0.3 deg^2, roughly 3 times the area of each very deep *Chandra* Deep Field. A total of 651 unique sources were detected in the four ACIS-I pointings in this field; 81 sources were detected in the soft but not in the full band, while 9 were detected only in the hard band. Roughly 15% of these 651 unique sources—118 sources in the soft band and 73 in the hard band—were previously detected in the CDF-S. The fluxes derived for these sources agree well with the fluxes obtained from the CDF-S observations.

The X-ray $\log N$-$\log S$ relation in the soft and hard bands agrees well with that derived from other X-ray surveys and with predictions of the most recent AGN population synthesis models for the X-ray background. As first discovered in early deep *Chandra* observations, we find in this sample that faint X-ray sources have in general harder spectra, indicating that these sources are likely obscured AGNs at moderate redshifts. This is predicted by AGN unification models that explain the properties of the X-ray background. A future paper will discuss the optical and near-IR properties of these objects. This field was observed with the *Spitzer Space Telescope* by the MIPS Guaranteed Time Observers (GTO) team and will also be observed by *Spitzer* as part of an approved program related to the MUSYC survey (PI: P. van Dokkum).

The source catalogs and images presented in this paper are available in electronic format on the World Wide Web .[18] We will continue to improve the source catalog as better calibration information, analysis methods, and software become available. For example, we plan to optimize the searching for variable sources and to study the multiwavelength properties of these X-ray sources.

Note added in manuscript.— After this paper was submitted, another catalog paper by Lehmer et al. (2005) appeared on astro-ph. Our results are similar, but the analysis assumptions are different and therefore the source catalogs differ, as do the papers. We expect the comparison to be useful.

We thank the referee for helpful comments that improved the manuscript and are grateful to Samantha Stevenson of the CXC Help Desk for her help and patience in answering our many questions regarding CIAO-related tools. We also acknowledge the help of Jeffrey Van Duyne in cross-correlating the X-ray and optical positions. This work was supported in part by NASA grant HST-GO-09425.13-A. E. T. would like to thank the support of Fundación Andes, Centro de Astrofísica FONDAP, and the Sigma Xi foundation through a Grant-in-Aid of Research. E. G. acknowledges support by the National Science Foundation under grant AST 02-01667, an NSF Astronomy and Astrophysics Postdoctoral Fellowship.

[18] See http://www.astro.yale.edu/svirani/ecdfs.

REFERENCES

Akiyama, M., et al. 2000, ApJ, 532, 700
Alexander, D. M., et al. 2003, AJ, 126, 539
Bauer, F. E., Alexander, D. M., Brandt, W. N., Schneider, D. P., Treister, E., Hornschemeier, A. E., & Garmire, G. P. 2004, AJ, 128, 2048
Brandt, W. N., et al. 2001, AJ, 122, 2810
Chandra X-Ray Center. 2005, The *Chandra* Proposers' Observatory Guide (Cambridge: CXC), http://ledas-cxc.star.le.ac.uk/proposer/POG/pog_c_pdf.html.
Ciliegi, P., Elvis, M., Wilkes, B. J., Boyle, B. J., & McMahon, R. G. 1997, MNRAS, 284, 401
Comastri, A., Setti, G., Zamorani, G., & Hasinger, G. 1995, A&A, 296, 1
Freeman, P. E., Kashyap, V., Rosner, R., & Lamb, D. Q. 2002, ApJS, 138, 185
Gawiser, E., et al. 2006, ApJS, 162, 1
Gehrels, N. 1986, ApJ, 303, 336
Gendreau, K. C., et al. 1995, PASJ, 47, L5
Giacconi, R., et al. 2001, ApJ, 551, 624
———. 2002, ApJS, 139, 369
Gilli, R., Risaliti, G., & Salvati, M. 1999, A&A, 347, 424
Gilli, R., Salvati, M., & Hasinger, G. 2001, A&A, 366, 407
Gioia, I. M., Maccacaro, T., Schild, R. E., Wolter, A., Stocke, J. T., Morris, S. L., & Henry, J. P. 1990, ApJS, 72, 567
Grant, C. E., Bautz, M. W., & Virani, S. N. 2002, in ASP Conf. Ser. 262, The High Energy Universe at Sharp Focus: *Chandra* Science, ed. E. M. Schlegel & S. D. Vrtilek (San Francisco: ASP), 401
Hasinger, G. 2004, Nucl. Phys. B Proc. Supp., 132, 86
Hornschemeier, A. E., et al. 2001, ApJ, 554, 742
Kenter, A. T., & Murray, S. S. 2003, ApJ, 584, 1016
Kim, D.-W., et al. 2004, ApJS, 150, 19
Kushino, A., et al. 2002, PASJ, 54, 327
Lehmer, B., et al. 2005, ApJS, 161, 21
Madau, P., Ghisellini, G., & Fabian, A. C. 1994, MNRAS, 270, L17
Marshall, F. E., et al. 1980, ApJ, 235, 4
Marshall, H. L., et al. 2004, Proc. SPIE, 5165, 497
Moretti, A., Campana, S., Lazzati, D., & Tagliaferri, G. 2003, ApJ, 588, 696
Nandra, K., & Pounds, K. A. 1994, MNRAS, 268, 405
Nandra, K., et al. 2005, MNRAS, 356, 568
Plucinsky, P. P., & Virani, S. N. 2000, Proc. SPIE, 4012, 681
Schwartz, D. A., & Virani, S. N. 2004, ApJ, 615, L21
Spergel, D. N., et al. 2003, ApJS, 148, 175
Stark, A. A., Gammie, C. F., Wilson, R. W., Bally, J., Linke, R. A., Heiles, C., & Hurwitz, M. 1992, ApJS, 79, 77
Strüder, L., et al. 2001, A&A, 365, L18
Townsley, L. K., Broos, P. S., Garmire, G. P., & Nousek, J. A. 2000, ApJ, 534, L139
Treister, E., & Urry, C. M. 2005, ApJ, 630, 115
Treister, E., et al. 2004, ApJ, 616, 123
Wang, J. X., et al. 2004, ApJ, 608, L21
Yang, Y., Mushotzky, R. F., Steffen, A. T., Barger, A. J., & Cowie, L. L. 2004, AJ, 128, 1501